Direct mapping from LES resolved scales to filtered-flame generated manifolds using convolutional neural networks

Andréa Seltz, Pascale Domingo, Luc Vervisch, Zacharias Nikolaou

Direct mapping from LES resolved scales to filtered-flame generated manifolds using convolutional neural networks

Andrea Seltz[a,b], Pascale Domingo[a], Luc Vervisch[a], Zacharias M. Nikolaou[c]

[a]*CORIA - CNRS, Normandie Université, INSA de Rouen, Technopole du Madrillet, BP 8 76801 Saint-Etienne-du-Rouvray, France*
[b]*Safran Aircraft Engines, Site de Villaroche, Rond-Point René Ravaud-Réau, 77550 Moissy Cramayel, France*
[c]*Defence and Security Research Institute, University of Nicosia, Nicosia, Cyprus.*

Abstract

A unified modelling framework for all unresolved terms in the filtered progress variable transport equation in large-eddy simulations of turbulent premixed flames is proposed, using convolutional neural networks. A direct numerical simulation database of a turbulent premixed stoichiometric methane/air jet flame is used in order to train convolutional neural networks to predict both the filtered progress variable source term and the unresolved scalar transport terms. A single variable readily available from the large-eddy simulation is required in order to calculate all inputs to networks, namely the Favre-filtered progress variable $\tilde{c}$. In the context of flame tabulated chemistry (premixed flamelet), the trained networks are shown to produce quantitatively good predictions of all unresolved terms in an apriori study, despite their different nature and irrespective of variations in filter size, without having to resort to solving any additional transport equations. The framework proposed in this study thus opens perspectives for the application of deep learning to the modeling of the non-linear aerothermochemistry equations which involve unresolved source and transport terms.

Keywords: Turbulent premixed combustion, Deep learning, Flamelet modelling, Flame tabulated chemistry, Machine learning, Neural networks

*Corresponding author
Email address: domingo@coria.fr (Pascale Domingo)

1. Introduction

In Large Eddy Simulation (LES), only the largest flow scales are resolved, while fluctuations of momentum, species concentration, and temperature below the mesh size are unknown. The effects of these unresolved scales appear as unclosed terms in the spatially-filtered governing equations and require modelling in order to obtain a closed system of equations [1].

With the rapid increase of computational resources and data storage capabilities in recent years, machine learning methods in general have had a tremendous impact in various fields such as speech, image and text recognition, robotics, and health-care amongst many others [2]. The modelling of unresolved terms in the highly non-linear transport equations of turbulent and reacting flows is a challenging and daunting task. The ability to "learn" from the data directly, presents a promising alternative given the abundance of data available both from simulations and experiments. Direct Numerical Simulation (DNS) databases where all flow and time scales are resolved, are of the order of Petabytes [3] and machine-learning methods are a natural tool for extracting useful information from these databases for modelling purposes.

In the context of turbulent combustion modelling, Artificial Neural Networks (ANNs) have been used mainly to deal with the introduction of complex chemistry in the simulations [4–8], or to manage complex multi-physics phenomena such as solid-fuel devolatilization [9]. Recently, Convolutional Neural Networks (CNNs), originally developed for analysing visual representations [10, 11], have been introduced as a tool for the direct deconvolution of the filtered progress variable [12], which combined with explicit filtering allowed the modelling of the unresolved variance, a key parameter in flamelet modeling [13]. CNNs were also used for modelling the unresolved flame surface wrinkling in [14] surpassing state of the art explicit algebraic models. CNNs have also been used to extract the chemical rate constant from shock-tube measurements [15] and for predicting the combustion activation energy [16].

A turbulent premixed stoichiometric methane/air jet flame is considered in this study

performing a priori evaluation of neural network based modeling from a fully resolved simulation, following a strategy combining CNNs with the pioneering works of Bray and co-workers [13, 17]. According to their analysis, the departure between the non-linear chemical sources as computed from the node values resolved on a coarse mesh (*i.e.*, neglecting unresolved fluctuations) and their space-filtered (or averaged) counterparts (*i.e.*, accounting for unresolved fluctuations), evolves with the local three-dimensional flame topology, convoluted with the level of mesh resolution, which controls the amplitude of the unresolved fluctuations of temperature and species.[1] Along these lines, we propose to explore the relationships between the three-dimensional distributions of chemical sources as computed from node values (thus a crude approximation of the filtered burning rates), and the filtered value of the non-linear source located at the center of this three-dimensional distribution, using a DNS database. The same procedure is adopted for the sum of the divergence of the unresolved part of the convective flux and of the molecular diffusive flux. The DNS database is then used to train convolutional networks in order to directly reconstruct the unresolved scalar sources and transport terms in the framework of tabulated detailed chemistry (premixed flamelet) LES. The major advantage of such a direct reconstruction of unresolved sources and fluxes from mesh-resolved quantities in the LES, is that by doing so there is no need for explicit filtering or solving additional transport equations, both of which save computational time and mitigate possible resolution issues [18].

2. Background and methodology

In chemistry tabulation based on premixed flame generated manifolds, all thermochemical quantities ϕ are uniquely related to an appropriate progress variable c (equal to unity in fully burnt products and vanishing in fresh gases), so that knowledge of the progress variable distribution $c(\underline{x}, t)$ is sufficient to characterise the reaction zones, *i.e.* $\phi(\underline{x}, t) = \phi(c(\underline{x}, t))$ [19–

[1] Bray and co-workers specifically focussed on the asymptotic limit where the mesh size is very large compared to the characteristic flame thickness.

22], including the burning rate

$$\dot{\omega}(\underline{x},t) = \dot{\omega}(c(\underline{x},t)) \,. \tag{1}$$

The progress variable may be defined from a set of species mass fractions, temperature, derived from optimisation [23–25] or following other strategies [26]. In any case, c should be a monotonic function through the laminar flamelet. In the context of LES, a transport equation for $\bar{\rho}\tilde{c}$ is solved,

$$\frac{\partial \overline{\rho}\tilde{c}}{\partial t} + \nabla \cdot (\overline{\rho}\tilde{\mathbf{u}}\tilde{c}) = \nabla \cdot (\overline{\rho} D_c(\tilde{c}) \nabla \tilde{c}) + \nabla \cdot \tau + \overline{\dot{\omega}} \,, \tag{2}$$

where ρ is the density, $\mathbf{u}$ is the velocity vector and $D_c(c)$ is the tabulated molecular diffusion coefficient of c, defined from the diffusion velocity of tabulated species (Eq. (15) in [27]). The notation $D_c(\tilde{c})$ means that the diffusion coefficient is here computed from the resolved filtered progress variable. $\overline{\dot{\omega}}(\underline{x},t)$ is the filtered burning rate of c. The sub-grid scale flux is

$$\tau = \tau_{D_c} - \tau_c \,, \tag{3}$$

where τ_{D_c} and τ_c are respectively the transport of c by unresolved fluctuations of molecular diffusive flux and momentum,

$$\tau_D = \overline{\rho D_c(c) \nabla c} - \overline{\rho} D_c(\tilde{c}) \nabla \tilde{c} \,, \tag{4}$$

$$\tau_c = \overline{\rho \mathbf{u} c} - \overline{\rho} \tilde{\mathbf{u}} \tilde{c} \,. \tag{5}$$

Numerous modeling strategies have been proposed in the literature for the unresolved terms of Eq. (2) in the context of tabulated chemistry, and a detailed review is given in [28]. Among those, many involve gradient transport models with an eddy viscosity hypothesis to close τ_c while τ_D is usually neglected.

Flamelet models for the burning rate $\overline{\dot{\omega}}$, are typically based on solving and additional balance equation for the variance of c, $c_v = \widetilde{c^2} - \tilde{c}\tilde{c}$. A function is then presumed for the

progress variable probability density function (pdf), which is parameterised using the two moments of c namely $\tilde{c}(\underline{x},t)$ and $c_v(\underline{x},t)$ [29–31]. A chemical lookup table is constructed using results from 1D flame simulations, and variables of interest are obtained using these two parameters from the table. For example, the filtered burning rate in Eq. (2) is closed using

$$\overline{\dot{\omega}}(\underline{x},t) = \int_0^1 \dot{\omega}(c^\star)\overline{P}(c^\star;\tilde{c}(\underline{x},t),c_v(\underline{x},t))dc^\star \,, \tag{6}$$

where $\overline{P}(c^*;\tilde{c}(\underline{x},t),c_v(\underline{x},t))$ is the presumed pdf. A characteristic length scale may also be added to the modeling framework, by combining the pdf with the Flame Surface Density (FSD) concept [32, 33]. In an attempt to account for the time history of micro-mixing, it has been proposed in [34] to include as a control parameter of the filtered thermo-chemistry lookup table, the age of fluid particles since their injection. Simulations coupling flame-generated manifolds with pdf transport using Eulerian stochastic fields have also been reported [35, 36]. The filtering of the tabulated one-dimensional flames is another option, providing closed expressions for τ_c and τ_D, in addition to $\overline{\dot{\omega}}$ [27, 37, 38]. More recently, deconvolution-based approaches have also been discussed and applied to the three terms $\overline{\dot{\omega}}$, τ_c and τ_D [39–43].

Overall, these modeling approaches directly or indirectly relate $\tilde{c}$ and $\nabla\tilde{c}$ to the unclosed terms. A slightly different approach is explored in this work. First, the statistical properties of $\overline{\dot{\omega}}$, τ_c and τ_D are examined using the results from the DNS database. Specific features are observed in the data connecting $\overline{\dot{\omega}}$ and $\nabla\cdot\tau = \nabla\cdot(\tau_D - \tau_c)$ to $\dot{\omega}(\tilde{c})$ and $\nabla\cdot(\overline{\rho}D_c(\tilde{c})\nabla\tilde{c})$ respectively, namely the burning rate and the divergence of the diffusive flux as computed from the resolved LES fields, *i.e.*, the node values over the LES mesh. ($\nabla\cdot(\overline{\rho}D_c(\tilde{c})\nabla\tilde{c})$ is already calculated when solving for $\tilde{c}$ and is thus available without additional computational cost.) These features suggest that image-type deep learning can be readily applied to dynamically determine two mapping functions $\mathcal{G}$ and $\mathcal{F}$ from convolutional neural networks

such that,

$$\overline{\dot{\omega}}(\underline{x},t) = \mathcal{G}\left[\dot{\omega}(\tilde{c}(\underline{x}_1,t)),\cdots,\dot{\omega}(\tilde{c}(\underline{x}_N,t))\right] , \quad (7)$$

$$\nabla\cdot\tau(\underline{x},t) = \mathcal{F}\left[\nabla\cdot\left(\overline{\rho}D_c(\tilde{c})\nabla\tilde{c}\right)(\underline{x}_1,t),\cdots,\nabla\cdot\left(\overline{\rho}D_c(\tilde{c})\nabla\tilde{c}\right)(\underline{x}_N,t)\right] , \quad (8)$$

where $\tilde{c}(\underline{x}_j,t)$ is known from the LES, with $\underline{x}_j$ the N points selected around $\underline{x}$ to build the input image of the networks. Note that the above relations are expressed in progress variable space *i.e.*, a single variable, $\tilde{c}$, is required in order to calculate the terms on the right-hand side of Eqs. (7) and (8) which constitute the inputs to the two networks $\mathcal{F}$ and $\mathcal{G}$. Provided $\mathcal{G}$ and $\mathcal{F}$ are known, Eq. (2) is fully closed without having to solve any additional transport equations. Also note that $\tilde{c}$ is a coordinate in which turbulent premixed flame properties are strongly depended on and feature a generic character when studied in c-space [13]. As a result, the dependence of relations (7) and (8) to the flow regime are expected to be weak as long as the networks are trained for conditions in a Borghi regime-diagram [44] close to the ones of the flames subsequently addressed by LES. This is also more likely to be the case, when $\mathcal{G}$ and $\mathcal{F}$ are determined from a reference turbulent premixed flame featuring a large degree of flame wrinkling, as is the case for the turbulent premixed jet-flame DNS database used in this study [41].

3. Direct simulation database

A previously developed methane-air stoichiometric premixed jet-flame DNS database [41, 45, 46] is used for training the neural networks. The configuration is shown in Fig. 1. The DNS database is obtained downstream of a well-resolved LES of a piloted premixed stoichiometric fuel-air jet, which generates turbulent flame conditions for the DNS inlet plane located 4.5 diameters downstream of injection. The LES and the DNS are run simultaneously and this is achieved by embedding, inside the LES mesh, a zone where the resolution is sufficiently high so as to resolve the thin reaction zones and the Kolmogorov length scale. The configuration is inspired from the experiment by Chen *et al.* [47]. This turbulent Bunsen

burner has a nozzle diameter of D = 12 mm, the jet Reynolds number is 24,000 (bulk nozzle velocity of 30 $\mathrm{m \cdot s^{-1}}$ and turbulent kinetic energy of 3.82 $\mathrm{m^2 \cdot s^{-2}}$). The pilot is set to fully burnt gases at $T_b = 2200$ K. The LES mesh consists of about 171 million nodes covering a domain 16D×8D×8D, with a resolution of the order of 150 μm (Fig. 1). The resolution in the DNS zone is fixed at 50 μm, which was calibrated to ensure a full resolution of the flow and flame scales for this jet flame having a Karlovitz number varying between 1 and 3 [41, 47]. Chemistry tabulation with a stoichiometric premixed flamelet with fresh gases at $T_o = 300$ K (GRI-3.0 mechanism [48] and progress variable defined from CO, CO_2, H_2O and NO_x as in [49]) is used for both LES and DNS, without any SGS modeling in the DNS part (SGS terms set to zero). The flame thermal thickness based on the progress variable field is of the order of $\delta_L \approx 400$ μm. The DNS zone consists of 28.58 million nodes (243×343×343), over a physical domain of 12 mm×18 mm×18mm. This DNS zone is located at $4.5D$ downstream of the nozzle, and at $5.5D$ the mesh is coarsened again to progressively resume the simulation using LES (Fig. 1). A progress variable presumed pdf approach is applied in the LES zones [29] and the SGS momentum fluxes are approximated with the Vreman model [50]. These simulations have been performed using the flow solver SiTCom [51], which solves the Navier-Stokes equations in their fully compressible form together with the balance equation for the filtered progress variable. The convective terms are discretised with a fourth-order centered skew-symmetric-like scheme [52] and the diffusive terms with a fourth-order centered scheme. Time is advanced explicitly with a third order Runge-Kutta method and NSCBC boundary conditions [53] are imposed at inlet and outlet, with the measured profiles with synthetic turbulence [54] prescribed at inlet. More details on the development and the use of this DNS database may be found in [41, 45, 46].

A Gaussian filtering operation, $G(\underline{x}) = (6/(\pi\Delta^2))^{3/2} \exp(-6\underline{x} \cdot \underline{x}/\Delta^2)$, with filter size $\Delta = 0.3$ mm $= 0.75\ \delta_L$, $\Delta = 0.6$ mm $= 1.50\ \delta_L$ and $\Delta = 0.9$ mm $= 2.25\ \delta_L$, is applied to the DNS variables in order to generate a priori LES filtered quantities, thus varying the resolution of the a priori fields from well-resolved to coarse LES (at least from the reaction

zone point of view, $\Delta = 0.9$ mm is 18 times larger than the DNS grid resolution).

4. Statistical analysis of unresolved terms

4.1. Turbulent flame properties

Figure 2 shows $\langle \overline{\dot{\omega}^+} \mid \tilde{c} \rangle$, the statistical mean over the DNS domain of the normalised filtered progress variable source, conditioned on values of $\tilde{c}$. The subscript '$^+$' denotes source terms normalised by their maximum value in the tabulated freely-propagating laminar premixed flame. The result obtained using a 1D laminar flame, $\dot{\omega}^+(\tilde{c})$, is shown as a solid line. As expected, the maximum of $\langle \overline{\dot{\omega}^+} \mid \tilde{c} \rangle$ decreases with increasing filter size and thus with increasing unresolved fluctuations [13]. Following the thickening of the filtered flame front, the response of this conditional filtered source term also spreads in progress variable space for increasing filter sizes, up to $\Delta = 0.9$ mm.

The statistical conditional means of $\langle \nabla \cdot \tau_c \mid \tilde{c} \rangle$ and of $\langle \nabla \cdot \tau_D \mid \tilde{c} \rangle$, the divergence of the convective and diffusive fluxes (Eqs. (4) and (5)), are shown in Fig. 3. The maximum level of velocity fluctuations observed in the fresh gases in the experiment at the streamwise location of the jet where the DNS zone is located (Fig. 1), is of the order of $u' = 1.80$ m$\cdot$s^{-1} [47]. Then, the ratio u'/S_L for this stoichiometric premixed methane-air flame is of the order of 5, with $S_L = 0.37$ m$\cdot$s^{-1}.

The number $N_B = [(T_b - T_o)/T_o]S_L/(2\alpha u')$, as defined by Veynante *et al.* [55], which differentiates between gradient transport, $N_B < 1$, $-\tau_c \propto \nabla\tilde{c}$, and counter-gradient transport, $N_B > 1$, $-\tau_c \propto -\nabla\tilde{c}$, in a Reynolds Averaged Navier Stokes context (RANS), is above unity in the present case for an efficiency factor $\alpha \leq 0.6$. The factor α in N_B accounts for the variability in the capability of turbulent eddies to wrinkle the reaction zone [55].

Considering space-filtered (LES) quantities, for $1 \leq \Delta/\delta_L \leq 3$, counter-gradient SGS transport was recently reported from DNS analysis for the same level of u'/S_L [43]. Overall, counter-gradient transport is found when $\nabla \cdot \tau_c$ and $\nabla^2\tilde{c}$ are of same sign. This is also what is observed in Fig. 3(a), with $\langle \nabla \cdot \tau_c \mid \tilde{c} \rangle$ negative on the burnt gas side where $\nabla^2\tilde{c} < 0$ and

$\langle \nabla \cdot \tau_c \mid \tilde{c} \rangle$ positive on the fresh side where $\nabla^2 \tilde{c} > 0$.[2] This behaviour is also observed in the scatter plot of the SGS convection divergence which is shown in Fig. 4, with the occurrence however of some negative values of $\nabla \cdot \tau_c$ around $\tilde{c} \rightarrow 0$, thus gradient transport in the preheat zone ensures the local flame propagation. On these scatter plots, the bounds of $\nabla \cdot \tau_c$ do not change much with the filter size Δ, but the spreading of the data for a given value of $\tilde{c}$ decreases with Δ.

The contribution of the SGS diffusive flux, $\nabla \cdot \tau_D$, in Fig. 3(b) cannot be neglected compared to the convective one, $\nabla \cdot \tau_c$, in Fig. 3(a). This would not be the case in the RANS context, where the SGS diffusive contribution would be inversely proportional to the turbulent Reynolds number of the flow, and thus could be neglected when compared to other transport terms [56]. The SGS diffusive fluxes in LES are actually inversely proportional to the turbulent Reynolds numbers of the LES mesh cells, based on the filter size and on the SGS velocity fluctuations. Therefore, the SGS turbulent Reynolds number appears too small for neglecting the divergence of τ_D. The response of the amplitude of $\langle \nabla \cdot \tau_D \mid \tilde{c} \rangle$ versus the filter size, is better understood by looking at the two terms $\left\langle \overline{\nabla \cdot (\rho D_c(c) \nabla c)} \mid \tilde{c} \right\rangle$ and $\langle \nabla \cdot (\overline{\rho} D_c(\tilde{c}) \nabla \tilde{c}) \mid \tilde{c} \rangle$ in Figs. 3(c) and 3(d). As expected, following the decay of the gradients with the increase of the filter size, these filtered transport terms decrease, leading to a decay of the amplitude of both the filtered and node-resolved diffusive budgets when Δ increases. In the case of $\langle \nabla \cdot (\overline{\rho} D_c(\tilde{c}) \nabla \tilde{c}) \mid \tilde{c} \rangle$ an almost self-similar behaviour is observed against Δ (Fig. 3(d)). This is not the case for $\left\langle \overline{\nabla \cdot (\rho D_c(c) \nabla c)} \mid \tilde{c} \right\rangle$, for which the response is also shifted against $\tilde{c}$ when Δ varies as one may observe from the results in Fig. 3(c). As a result, the difference between these two terms, $\nabla \cdot \tau_D$, is not monotonic against Δ (Fig. 3(b)). It is important also to note that the thickening of the flame front in physical space resulting from filtering, directly impacts these budgets here visualised in $\tilde{c}$-space. Finally, the sum of SGS fluxes $\langle \nabla \cdot \tau \mid \tilde{c} \rangle = \langle \nabla \cdot (\tau_D - \tau_c) \mid \tilde{c} \rangle$, which combines responses of both unresolved

[2] Almost zero fluxes on the burnt gas side appear before $\widetilde{c} = 1$, because of the choice of the progress variable as in Godel et al. [49], which is designed as slowly varying approaching burnt gases to preserve a single-valued response of NOx versus progress variable.

convection and molecular diffusion, is shown in Fig. 5.

4.2. Physical arguments for CNN training

As will be explained later in the text, two CNN will be used to approximate respectively the values of $\nabla \cdot \tau(\underline{x}, t)$ and $\overline{\dot{\omega}}(\underline{x}, t)$ from an input composed of a set of data (images). In practice, this is done by interpolating over a large number of relationships between 'images' and 'labels', which were the values of $\nabla \cdot \tau(\underline{x}, t)$ and $\overline{\dot{\omega}}(\underline{x}, t)$ "learned" during a training phase. Here the inputs (images) are composed of $\dot{\omega}(\tilde{c}(\underline{x}_j, t))$ and $\nabla \cdot \left(\overline{\rho} D_c(\tilde{c}) \nabla \tilde{c}\right)(\underline{x}_j, t)$ for $j = 1, \cdots, N$, where N is the number of points surrounding a point $\underline{x}$, where the values of $\overline{\dot{\omega}}(\underline{x}, t)$ and $\nabla \cdot \tau(\underline{x}, t)$ are sought.

The input set of data should feature specific topological properties, which can be extracted by convoluting the data points with a series of filters and specific operations. Figure 6 shows $\left\langle \overline{\dot{\omega}^+} \mid \tilde{c} \right\rangle$ versus $\dot{\omega}^+(\tilde{c})$ for different filter sizes and Fig. 7 illustrates the image-label relationship which could be implemented. Notice that the CNN will not operate on the statistical conditional means in the end, but directly on the raw data, however initiating the analysis at the statistical level helps to select the variables. As one may observe from Fig. 6, the filtered source term is not a single-valued function of the node resolved source, nevertheless accounting also for the local curvature of the data set as one of the features, should be sufficient to build a one-to-one response. Obviously, this constitutes only a very preliminary condition to secure the determination of the function $\mathcal{G}$ of Eq. (7) and more features will need to be extracted on the full set of turbulent data, as discussed thereafter. Because of non-deterministic local sub-grid scale wrinkling of the flame surface, the relation between $\dot{\omega}^+(\tilde{c})$ and $\overline{\dot{\omega}^+}$ is actually scattered as shown in Fig. 8, with some deviation from the response seen in Fig. 6, and this scattering should be reproduced by a reliable physical model. This is where numerical modelling can take great benefit from deep learning, which automatically discovers the most relevant signal features through elementary operations, to then allow for interpolating over the very large dataset learned.

Similarly, Fig. 9 shows $\langle \nabla \cdot \tau \mid \tilde{c} \rangle$ versus $\langle \nabla \cdot \left(\overline{\rho} D_c(\tilde{c}) \nabla \tilde{c}\right) \mid \tilde{c} \rangle$ and Fig. 10 the full set of

data $\nabla \cdot \tau$ versus $\nabla \cdot (\overline{\rho} D_c(\tilde{c}) \nabla \tilde{c})$, revealing a dataset which can easily be analysed by CNNs for identifying the function $\mathcal{F}$ in Eq. (8). It will be seen thereafter that this is a valid option for the case considered. Because momentum also contributes to $\nabla \cdot \tau$, an alternative would consist of introducing information on velocity in the $\mathcal{F}$ neural network (Eq. (8)). An option that was not found necessary in the present study where both SGS convective and diffusive fluxes are combined to build a single CNN for the divergence of fluxes. For this set of data, various options in terms of neural network layers number and filtering kernels have been tried. Best results were obtained with two layers and the set of kernels and data organisation now reported.

5. CNN training process

The LES mesh size required to resolve with $n = 5$ points the filtered progress variable signal, may be estimated from $h = (\Delta/n)\sqrt{\pi/6 + \delta_L^2/\Delta^2}$ [42]. A three-dimensional test-box of size $(2h)^3$ is constructed around every of the M = 28.58 million DNS nodes. This test box is centered at $\underline{x}$ and contains $N = 27$ points which hold the three-dimensional distributions of $\dot{\omega}(\tilde{c}(\underline{x}_j, t))$ and $\nabla \cdot (\overline{\rho} D_c(\tilde{c}) \nabla \tilde{c})\,(\underline{x}_j, t)$, for $j = 1, \cdots, N$. These data are stored and constitute the 'images' that will be processed by the CNN as shown in Fig. 11. The 'labels' of each i-th image are $\overline{\dot{\omega}}[i] = \overline{\dot{\omega}}(\underline{x}, t)$ and $\nabla \cdot \tau[i] = \nabla \cdot (\tau_D(\underline{x}, t) - \tau_c(\underline{x}, t))$ for $i = 1, \cdots, N_L$. Two networks of similar structures (same number of layers, convolution kernels, etc.) are trained, one for the chemical source and one for the SGS fluxes.

To reduce the computational cost, only part of the database is used for training. For each value of Δ, the following procedure is applied:

- First, 1000 images with their associated i-th label are built. 20 values of $c^\star$ uniformly distributed between 0 and 1 ($\Delta c^\star = 0.05$) are defined. For each value of $c^\star$, 50 images are randomly selected so that $\tilde{c}(\underline{x}, t) \in [c^\star - \Delta c^\star/2; c^\star + \Delta c^\star/2]$ ($\underline{x}$ denotes the center of the test box, Fig. 11).

- Overfitting is avoided by adding uncorrelated random perturbations to the images, $\dot{\omega}(\tilde{c}(\underline{x}_j,t))$ and $\nabla\cdot\left(\overline{\rho}D_c(\tilde{c})\nabla\tilde{c}\right)(\underline{x}_j,t)$, as 10% of their maximum in the test box, to build a second image for each label. 2000 images are then available for 1000 labels.

Finally, the database used for training with two filter sizes contains 4000 images and $N_L =$ 2000 labels. Hence, for every quantity studied, a set of 27×4000 =108000 data ($\dot{\omega}(\tilde{c}(\underline{x}_j,t))$ and $\nabla\cdot\left(\overline{\rho}D_c(\tilde{c})\nabla\tilde{c}\right)(\underline{x}_j,t)$) is involved, associated to the 2000 reference labels ($\overline{\dot{\omega}}[i]$ and $\nabla\cdot\tau[i]$ for $i=1,\cdots,N_L$).

A series of convolution/sampling operations are done iteratively during the training phase, in which the neural weights are adjusted until a satisfying minimal error is obtained between the value of $\nabla\cdot\tau(\underline{x},t)$ and $\overline{\dot{\omega}}(\underline{x},t)$ used for training (labels) and the values returned by the neural networks prediction. Convolution/sampling operations are thus performed on the database to extract its features using a number of different kernels [10, 11]:

1. Each image is convoluted with 32 different filter kernels obtained with random values from a truncated normal distribution. Meaningful values of the obtained features are then extracted with a max pooling non-linear function to avoid excessive computational costs.
2. The process is repeated with 64 filters, decomposing the image into several meaningful features, which is useful for seeking out the inner properties of the fluxes and sources.
3. Two fully connected layers are built to process the 64 obtained features, and to classify the image according to the learned labels. The probabilities linking this image to each of the learned labels are then known in the form of coefficients ranging between zero and unity.

The training of the network was conducted using the TensorFlow (www.tensorflow.org) library and breakdown of the network structure is given in Fig. 12. During this training phase, a 50% drop-out rate is applied, *i.e.*, 2000 images are randomly selected at every iteration and about 100 iterations (or 'epoch') are needed to reach convergence. The error function used for training is based on cross entropy [57], while the training is controlled by the Adam

optimizer [58] for stochastic gradient descent, with a user-defined learning rate of 10^{-4}. Both normalised and non-normalised input ($\dot{\omega}(\tilde{c})$ and $\nabla\cdot(\overline{\rho}D_c(\tilde{c})\nabla\tilde{c})$) and output values ($\overline{\dot{\omega}}$ and $\nabla\cdot\tau$) of networks have been used, without much difference, results are presented for the non-normalised training.

6. CNN mapping of fluxes and sources from LES resolved fields

In using the networks, the $N = 27$ values of the chemical sources and of the divergence of the fluxes computed from the resolved progress variable field in the test box surrounding the LES cell (Fig. 11), constitute the input. In this feasibility study, for each filter size, 1000 filtered DNS fields are used for a priori tests (the noised images introduced during the training phase do not enter these tests). The unknown terms are then approximated from interpolation over the $N_L = 2000$ labels values ($\overline{\dot{\omega}}[i]$ and $\nabla\cdot\tau[i]$) of the training phase,

$$\begin{aligned}
\overline{\dot{\omega}}(\underline{x},t) &= \mathcal{G}\left[\dot{\omega}(\tilde{c}(\underline{x}_1,t)),\cdots,\dot{\omega}(\tilde{c}(\underline{x}_N,t))\right] \\
&= \sum_{i=1}^{N_L} P_i(\underline{x},t)\times\overline{\dot{\omega}}[i]\,, \qquad (9)\\
\nabla\cdot\tau(\underline{x},t) &= \mathcal{F}\left[\nabla\cdot\left(\overline{\rho}D_c(\tilde{c})\nabla\tilde{c}(\underline{x}_1,t)\right),\cdots,\nabla\cdot\left(\overline{\rho}D_c(\tilde{c})\nabla\tilde{c}(\underline{x}_N,t)\right)\right] \\
&= \sum_{i=1}^{N_L} T_i(\underline{x},t)\times\nabla\cdot\tau[i]\,, \qquad (10)
\end{aligned}$$

where $P_i(\underline{x},t)$ and $T_i(\underline{x},t)$, both $\in[0,1]$, are the probability that the image belongs to the label 'i', as returned by the neural networks $\mathcal{G}$ and $\mathcal{F}$. In practice, the modelled filtered sources and divergence of SGS fluxes are thus non-linearly interpolated, according to the local LES resolved flame topology, over 2000 reference DNS values.

The training is performed for the smaller and largest filter sizes *i.e.*, $\Delta = 0.3$ mm and $\Delta = 0.9$ mm. Then, the prediction capabilities of the obtained CNN are tested a priori for these filter sizes and for intermediate values of $\Delta\in[0.3,0.9]$, for which this network has not been trained (so-called 'untrained case'). Notice that the ratio of three between the filter sizes used for training can be considered large, as these filters vary between 0.75 δ_L and

2.25 δ_L. This ratio of more than one flame thickness is here intentional to test the method in the limit case where the neural networks are used for filter sizes far from those of their training.

Using GPU 'NVDIA Pascal', the training of the fluxes requires 4 hours. Compared to the fluxes, the filtered source terms have a larger range of variation between the two filter sizes used for training and they require 24 hours of training on the same GPU. Once trained, the network may be used directly in a flow-solver for a CPU cost of about the one required with a turbulent combustion closure based on chemistry tabulation and presumed probability density function [29].

The averages of the predicted divergence of the unresolved fluxes conditioned on the progress variable, $\langle \nabla \cdot \tau \mid \tilde{c} \rangle$, are first compared against the filtered DNS in Fig. 13. The CNN reproduces the expected behaviour and amplitude of $\nabla \cdot \tau$, the fluctuations are also well captured, as seen in Fig 14. (Note that because the binning intervals to compute conditional means are different than in Fig. 5, the extrema also differ.) The test for the untrained filter level is performed with a filter size $\Delta = 0.45$ mm $= 1.125\delta_L$. This constitutes a stringent test case, because neural networks are known to be prone to rapid divergence when applied away from their training area. However, staying within the bounds of the training filter sizes, Fig. 13(b) shows that the response of the divergence of the unresolved fluxes is well captured. The plots showing conditional fluctuations in Fig. 14(b) confirm this moderate deviation from the reference filtered DNS. These results need to be put in perspective with predictions of unresolved fluxes using most advanced SGS models, where sometimes even the sign is not properly returned (see for instance Fig. 8 of [43] reporting strong departure from DNS in SGS transport modeling in turbulent premixed flames).

Similar results are obtained for the filtered source terms, which are shown in Figs. 15 and 16. For the trained filter sizes ($\Delta = 0.3$ and 0.9 mm), the filtered chemical source as predicted by the CNN matches the DNS reference, specifically for the largest filter, with a good reproduction of the parabolic shape. The conditional fluctuations of filtered burning

rates are also well captured (Fig. 16). For the untrained case however, some departure from the DNS value is observed, but still reasonable, at least comparable to what could be expected using classic models to estimate the filtered source terms. This would particularly be the case against formulations where the Arrhenius form is kept at the resolved scales after simply applying a scaling factor, thus far from the parabolic shape developing with the increase in filter size. In a previous work [41], modeling of the filtered source based on 3D approximate deconvolution and 1D flame deconvolution was tested against the same DNS database. As shown in Fig.17(b) of [41], the error on the burning rate estimation conditioned on the progress variable could reached up to 25% for $\Delta = 3\delta_L$. In the present case with the neural network, the maximum error is of the order of 1% on the trained database and of 16% for the untrained ones, confirming the potential of the approach.

7. Conclusion

A novel modelling framework using machine-learning is proposed for providing closures for all unresolved terms in the filtered transport equation of the progress variable in large-eddy simulations of turbulent premixed flames in the context of flamelet tabulated chemistry. A turbulent premixed methane/air stoichiometric premixed jet flame is considered and a priori evaluation of modeling based on neural networks is performed.

Convolutional neural networks are trained using data from a direct numerical simulation database, in order to predict the filtered progress-variable source term, and the unresolved fluxes in the filtered transport equation of $\tilde{c}$. The advantage of the approach proposed in this study, is that a single variable which is readily available, $\tilde{c}$, is required in order to calculate all inputs to networks, without having to resort to solving any additional transport equations for modelling all terms in the transport equation. The convolutional neural networks are shown to provide quantitatively accurate predictions of both the source and flux terms, which are two substantially different terms and otherwise difficult to model in a single unified framework. The predictions capabilities of the networks are also demonstrated to be only

weakly insensitive to variations in filter width, which is an important attribute for any sub-grid scale model. Because they are based on the progress variable, a generic parameter of premixed flames, the networks should perform well for any turbulent premixed flame located in the Borghi regime-diagram close to the conditions used for training. However, as a non-linear interpolation tool of high-dimensionality, it cannot perform well for cases with operating conditions far from those of training.

Acknowledgment

The PhD of the first author is funded by ANRT (Agence Nationale de la Recherche et de la Technology), SAFRAN-AE under the CIFRE No 1643/2016. Computing time has been provided by CRIANN (Centre Régional Informatique et d'Applications Numériques de Normandie). This work was granted access to the HPC resources of IDRIS-CNRS under the allocation 2018-A0052B00152 made by GENCI (Grand Equipement National de Calcul Intensif).

References

[1] H. Pitsch, Large Eddy Simulation of Turbulent Combustion, Annual Review of Fluid Mechanics 38 (2006) 453–482.

[2] R. Wason, Deep learning: Evolution and expansion, Cognitive Systems Research 52 (2018) 701–708.

[3] K. Kanov, R. Burns, C. Lalescu, G. Eyink, The Johns Hopkins turbulence databases: an open simulation laboratory for turbulence research, Comput. Sci. Eng. 17 (2015) 10–17.

[4] J. A. Blasco, N. Fueyo, C. Dopazo, J. Ballester, Modelling the temporal evolution of a reduced combustion chemical system with artificial neural network, Combust. Flame 113 (1-2) (1998) 38–52.

[5] F. C. Christo, A. R. Masri, E. M. Nebot, Artificial neural network implementation of chemistry with pdf simulation of H2/CO2 flames, Combust. Flame 106 (1996) 406–427.

[6] B. A. Sen, E. R. Hawkes, S. Menon, Large eddy simulation of extinction and reignition with artificial neural networks based chemical kinetics, Combust. Flame 157 (3) (2010) 566–578.

[7] B. A. Sen, S. Menon, Large eddy mixing based tabulation and artificial neural networks for large eddy simulations of turbulent flames, Combust. Flame 157 (1) (2010) 62–74.

[8] L. L. Franke, A. K. Chatzopoulos, S. Rigopoulos, Tabulation of combustion chemistry via Artificial Neural Networks (ANNs): Methodology and application to LES-PDF simulation of Sydney flame L, Combust. Flame 185 (2017) 245–260.

[9] T. Abbas, M. M. Awai, F. C. Lockwood, An artificial intelligence treatment of devolatilization for pulverized coal and biomass in co-fired flames, Combust. Flame 132 (3) (2003) 305–318.

[10] Y. Lecun, Y. Bengio, G. Hinton, Deep learning, Nature 521 (2015) 436–444.

[11] J. Schmidhuber, Deep learning in neural networks: An overview, Neural Networks 61 (2015) 85–117.

[12] Z. Nikolaou, C. Chrysostomou, L. Vervisch, S. Cant, Modelling turbulent premixed flames using convolutional neural networks: application to sub-grid scale variance and filtered reaction rate, Flow Turbulence Combust. (in press) .

[13] K. N. C. Bray, The Challenge of turbulent combustion, Symp. (Int.) on Combust. 26 (1996) 1–26.

[14] C. J. Lapeyre, A. Misdariis, N. Cazards, D. Veynante, T. Poinsot, Training convolutional neural networks to estimate turbulent sub-grid scale reaction rates, Combust. Flame 203 (2019) 255–264.

[15] R. Ranade, S. Alqahtani, A. Farooq, T. Echekki, An ANN based hybrid chemistry framework for complex fuels, Fuel 241 (2019) 625–636.

[16] W. Jiang, X. Xing, X. Zhang, M. Mi, Prediction of combustion activation energy of

NaOH/KOH catalyzed straw pyrolytic carbon based on machine learning, Renewable energy 130 (2019) 1216–1225.

[17] J.-B. Moss, K. Bray, A unified statistical model of the premixed turbulent flame, Acta Astronautica 4 (1977) 291–319.

[18] C. Mehl, J. Idier, B. Fiorina, Evaluation of deconvolution modelling applied to numerical combustion, Combust. Theory Modelling 22 (1) (2018) 38–70.

[19] O. Gicquel, N. Darabiha, D. Thevenin, Laminar Premixed Hydrogen / Air Counterflow Flame Simulations Using Flame Prolongation of ILDM With Differential Diffusion, Proc. Comb. Inst. 28 (2000) 1901–1908.

[20] J. A. van Oijen, F. A. Lammers, L. P. H. de Goey, Modeling of Complex Premixed Burner Systems by Using Flamelet-Generated Manifolds, Combust. Flame 127 (3) (2001) 2124–2134.

[21] P.-D. Nguyen, L. Vervisch, V. Subramanian, P. Domingo, Multidimensional flamelet-generated manifolds for partially premixed combustion, Combust. Flame 157 (1) (2010) 43–61.

[22] A. Scholtissek, P. Domingo, L. Vervisch, C. Hasse, A self-contained progress variable space solution method for thermochemical variables and flame speed in freely-propagating premixed flamelets, Proc. Combust. Inst. 27 (2) (2019) 1529–1536.

[23] Y.-S. Niu, L. Vervisch, P. D. Tao, An optimization-based approach to detailed chemistry tabulation: Automated progress variables definition, Combust. Flame 160 (4) (2013) 776–785.

[24] U. Prufert, S. Hartl, F. Hunger, D. Messig, M. Eiermann, C. Hasse, A constrained control approach for the automated choice of an optimal progress variable for chemistry tabulation, Flow Turbulence Combust. 94 (3) (2015) 593–617.

[25] M. Ihme, L. Shunn, J. Zhang, Regularization of reaction progress variable for application to flamelet-based combustion models, J. Comput. Phys. 231 (2012) 7715–7721.

[26] M.-S. Benzinger, R. Schiessl, U. Maas, A versatile coupled progress variable / REDIM

model for auto-ignition and combustion, Proc. Combust. Inst. 36 (3) (2017) 3613–3621.

[27] S. Nambully, P. Domingo, V. Moureau, L. Vervisch, A Filtered-Laminar-Flame PDF sub-grid scale closure for LES of premixed turbulent flames. Part I: Formalism and application to a bluff-body burner with differential diffusion, Combust. Flame 161 (7) (2014) 1756–1774.

[28] J. A. van Oijen, A. Donini, R. J. M. Bastiaans, J. H. M. tenThije Boonkkamp, L. P. H. de Goey, State-of-the-art in premixed combustion modeling using flamelet generated manifolds, Progress Energy Combust. Sci. 57 (2016) 30 – 74.

[29] P. Domingo, L. Vervisch, D. Veynante, Large-Eddy Simulation of a lifted methane-air jet flame in a vitiated coflow, Combust. Flame 152 (3) (2008) 415–432.

[30] V. Subramanian, P. Domingo, L. Vervisch, Large-eddy simulation of forced ignition of an annular bluff-body burner, Combust. Flame 157 (3) (2010) 579–601.

[31] J. Lai, N. Chakraborty, Modeling of progress variable variance transport in head-on quenching of turbulent premixed flames: A direct numerical simulation analysis, Combust. Sci. Tech. 188 (11-12) (2016) 1925–1950.

[32] G. Lecocq, S. Richard, O. Colin, L. Vervisch, Hybrid presumed pdf and flame surface density approach for Large-Eddy Simulation of premixed turbulent combustion, Part 1: Formalism and simulations of a quasi-steady burner, Combust. Flame 158 (6) (2011) 1201–1214.

[33] G. Lecocq, S. Richard, O. Colin, L. Vervisch, Hybrid presumed pdf and flame surface density approach for Large-Eddy Simulation of premixed turbulent combustion, Part 2: Early flame development after sparking, Combust. Flame 158 (6) (2011) 1215–1226.

[34] N. Enjalbert, P. Domingo, L. Vervisch, Mixing time-history effects in Large Eddy Simulation of non-premixed turbulent flames: Flow-Controlled Chemistry Tabulation, Combust. Flame 159 (1) (2012) 336–352.

[35] L. Valino, A field monte carlo formulation for calculating the probability density function of a single scalar in turbulent flow, Flow Turbulence Combust. 60 (2) (1998) 157–172.

[36] A. Avdić, G. Kuenne, J. Janicka, Flow physics of a bluff-body swirl stabilized flame and their prediction by means of a joint Eulerian stochastic field and tabulated chemistry approach, Flow Turbulence Combust. 97 (4) (2016) 1185–1210.

[37] B. Fiorina, R. Vicquelin, P. Auzillon, N. Darabiha, O. Gicquel, D. Veynante, A filtered tabulated chemistry model for LES of premixed combustion, Combust. Flame 157 (2010) 465–475.

[38] R. Mercier, T. Schmitt, D. Veynante, B. Fiorina, The influence of combustion SGS submodels on the resolved flame propagation. Application to the LES of the Cambridge stratified flames, Proc. Combust. Inst. 35 (2) (2015) 1259–1267.

[39] P. Domingo, L. Vervisch, Large Eddy Simulation of premixed turbulent combustion using approximate deconvolution and explicit flame filtering, Proc. Combust. Inst. 35 (2) (2015) 1349–1357.

[40] Q. Wang, M. Ihme, Regularized deconvolution method for turbulent combustion modeling, Combust. Flame 176 (2017) 125–142.

[41] P. Domingo, L. Vervisch, DNS and approximate deconvolution as a tool to analyse one-dimensional filtered flame sub-grid scale modeling, Combust. Flame 177 (2017) 109–122.

[42] Z. Nikolaou, L. Vervisch, A priori assessment of an iterative deconvolution method for LES sub-grid scale variance modelling, Flow Turbulence Combust. 101 (1) (2018) 33–53.

[43] Z. Nikolaou, R. S. Cant, L. Vervisch, Scalar flux modelling in turbulent flames using iterative deconvolution, Phys. Rev. Fluids. 3 (4) (2018) 043201.

[44] R. Borghi, Mise au point sur la structure des flammes turbulentes, J. Chimie Physique 81 (6) (1984) 361–370.

[45] L. Cifuentes, C. Dopazo, J. Martin, P. Domingo, L. Vervisch, Local volumetric dilatation rate and scalar geometries in a premixed methane-air turbulent jet flame, Proc. Combust. Inst. 35 (2) (2015) 1295–1303.

[46] L. Cifuentes, C. Dopazo, J. Martin, P. Domingo, L. Vervisch, Effects of the local flow

topologies upon the structure of a premixed methane-air turbulent jet flame, Flow Turbulence Combust. 96 (2) (2016) 535–546.

[47] Y.-C. Chen, N. Peters, G. A. Schneemann, N. Wruck, U. Renz, M. S. Mansour, The detailed flame structure of highly stretched turbulent premixed methane-air flames, Combust. Flame 107 (3) (1996) 223–244.

[48] G. P. Smith, D. M. Golden, M. Frenklach, N. W. Moriarty, B. Eiteneer, M. Goldenberg, C. T. Bowman, R. K. Hanson, S. Song, W. C. Gardiner, V. V. Lissianski, Z. Qin, Tech. Rep., http://www.me.berkeley.edu/gri-mech/, 1999.

[49] G. Godel, P. Domingo, L. Vervisch, Tabulation of NOx chemistry for Large-Eddy Simulation of non-premixed turbulent flames, Proc. Combust. Inst. 32 (2009) 1555–1561.

[50] A. W. Vreman, An eddy-viscosity subgrid-scale model for turbulent shear flow: Algebraic theory and applications, Phys. Fluids. 16 (10) (2004) 3670–3681.

[51] L. Bouheraoua, P. Domingo, G. Ribert, Large-eddy simulation of a supersonic lifted jet flame: Analysis of the turbulent flame base, Combust. Flame 179 (2017) 199–218.

[52] F. Ducros, F. Laporte, T. Soulères, V. Guinot, P. Moinat, B. Caruelle, High-order fluxes for conservative skew-symmetric-like schemes in structured meshes: application to compressible flows, J. Comput. Phys. 161 (2000) 114–139.

[53] G. Lodato, P. Domingo, L. Vervisch, Three-dimensional boundary conditions for Direct and Large-Eddy Simulation of compressible viscous flows, J. Comput. Phys 227 (10) (2008) 5105–5143.

[54] M. Klein, A. Sadiki, J. Janicka, A digital filter based generation of inflow data for spatially developing direct numerical or large eddy simulations, J. Comp. Physics 186 (2) (2002) 652–665.

[55] D. Veynante, A. Trouvé, K. Bray, T. Mantel, Gradient and counter-gradient scalar transport in turbulent premixed flames, J. Fluid Mech. 332 (1997) 263–293.

[56] D. Veynante, L. Vervisch, Turbulent Combustion Modeling, Prog Energy Combust Sci 28 (2002) 193–266.

[57] P.-T. de Boer, D. P. Kroese, S. S. Mannor, R. Y. Rubinstein, A tutorial on the cross-entropy method, Annals Operations Research 134 (1) (2005) 19–67.

[58] D. P. Kingma, J. L. Ba, ADAM: A method for stochastic optimization, https://arxiv.org/pdf/1412.6980, 2017.

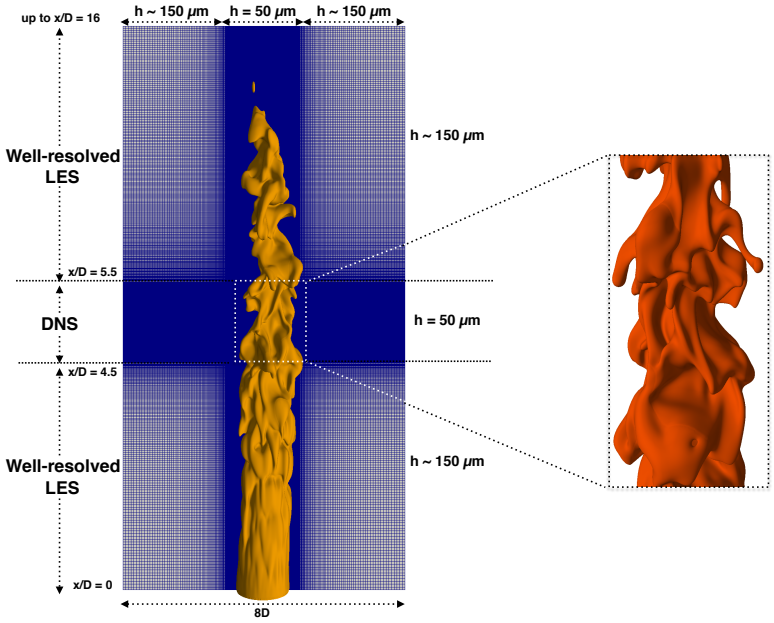

Figure 1: LES-DNS snapshot of the jet-flame simulation [41]. Mesh and iso-progress variable $c = 0.8$. h: resolution. Red iso-surface: zoom of iso-$c = 0.8$ in the DNS zone (different angle view).

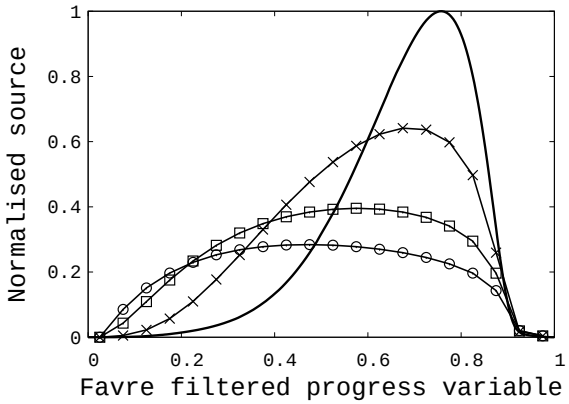

Figure 2: Thick-line: $\dot{\omega}^+(\tilde{c})$ vs $\tilde{c}$ as obtained from a 1D laminar flame (tabulated chemistry). $\left\langle \overline{\dot{\omega}^+} \mid \tilde{c} \right\rangle$ from DNS vs $\tilde{c}$ for filter sizes $\times$: 0.3 mm, $\square$: 0.6 mm, $\circ$: 0.9 mm ($\delta_L = 0.4$ mm).

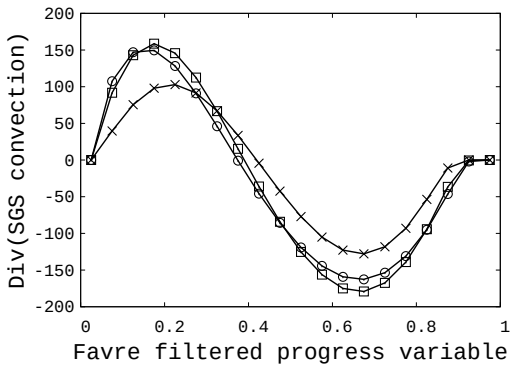

(a) $\langle \nabla \cdot \tau_c \mid \tilde{c} \rangle$

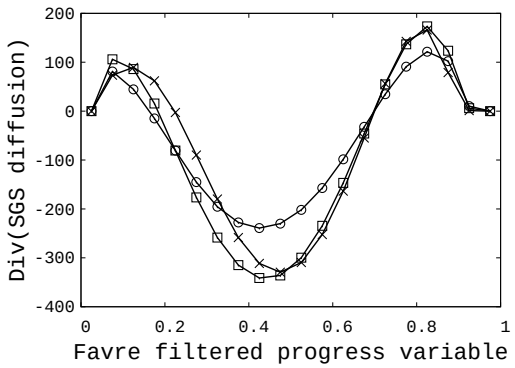

(b) $\langle \nabla \cdot \tau_D \mid \tilde{c} \rangle$

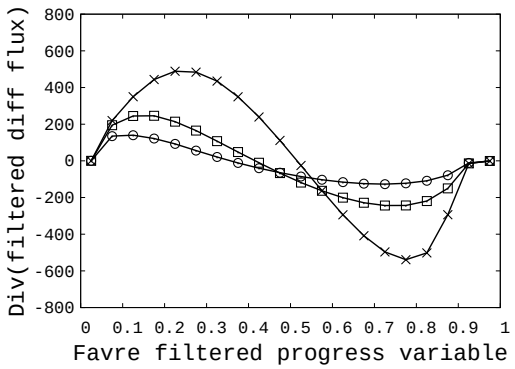

(c) $\left\langle \overline{\nabla \cdot (\rho D_c(c) \nabla c)} \mid \tilde{c} \right\rangle$

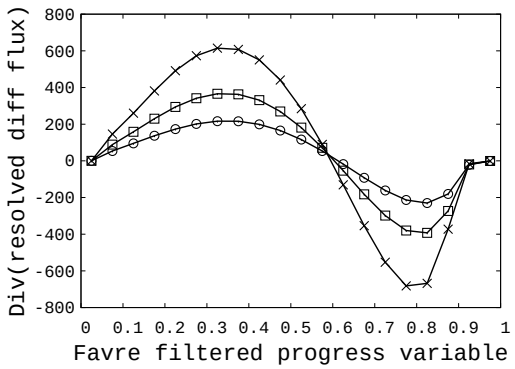

(d) $\langle \nabla \cdot (\overline{\rho} D_c(\tilde{c}) \nabla \tilde{c}) \mid \tilde{c} \rangle$

Figure 3: Conditional statistical means vs filtered progress variable. (a): Divergence of SGS convective scalar flux. (b): divergence of SGS diffusive flux. (c): filtered diffusive flux. (d): diffusive flux computed from the resolved quantities. Filter size $\times$: 0.3 mm, $\square$: 0.6 mm, $\circ$: 0.9 mm.

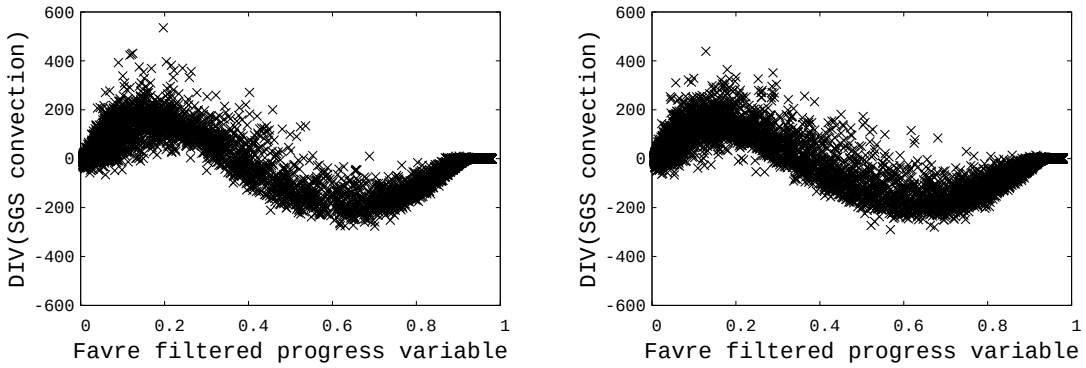

(a) $\Delta = 0.6$ mm (b) $\Delta = 0.9$ mm

Figure 4: Scatter plot of $\nabla \cdot \tau_c$ (1 every 100 DNS points shown).

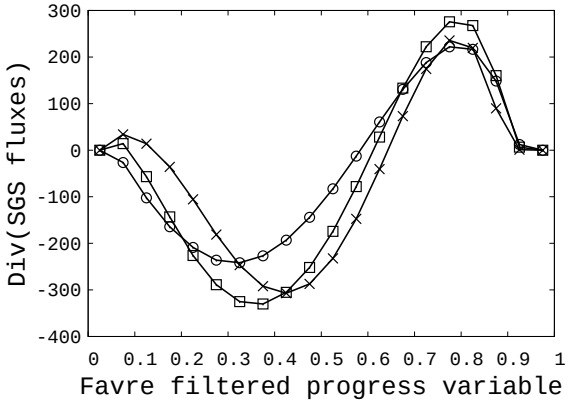

Figure 5: $\langle \nabla \cdot \tau \mid \tilde{c} \rangle = \langle \nabla \cdot (\tau_D - \tau_c) \mid \tilde{c} \rangle$ vs $\tilde{c}$. Filter size $\times$: 0.3 mm, $\square$: 0.6 mm, $\circ$: 0.9 mm.

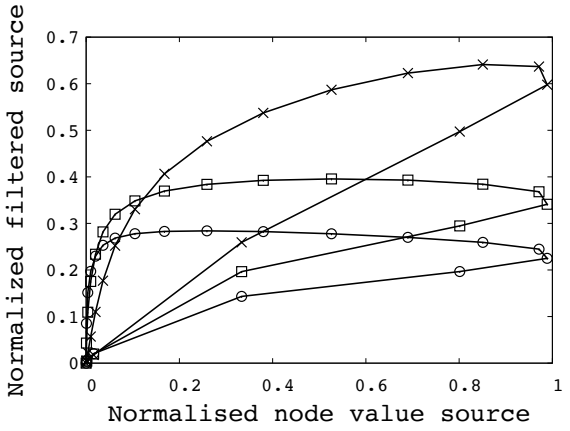

Figure 6: $\left\langle \overline{\dot{\omega}^{+}}(c) \mid \tilde{c} \right\rangle$ vs $\dot{\omega}^{+}(\tilde{c})$. Filter size $\times$: 0.3 mm, $\square$: 0.6 mm, $\circ$: 0.9 mm.

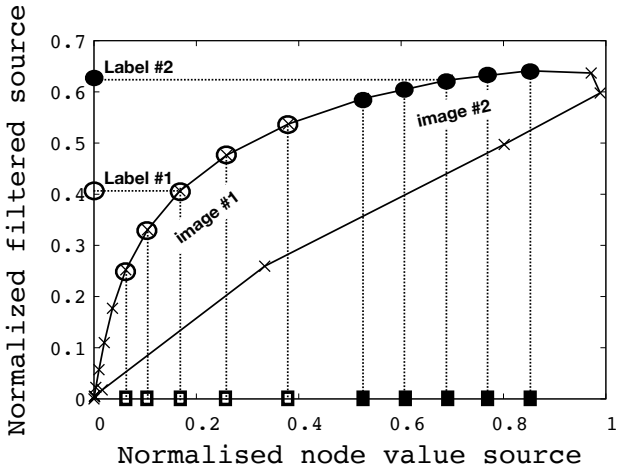

Figure 7: $\left\langle \overline{\dot{\omega}^{+}}(c) \mid \tilde{c} \right\rangle$ vs $\dot{\omega}^{+}(\tilde{c})$. Sketch of the construction of images and labels for training a CNN. Filter size: 0.3 mm.

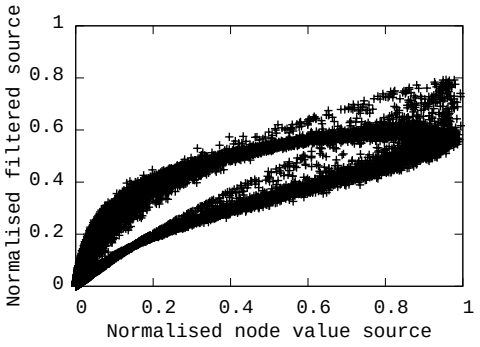

(a) $\Delta = 0.3$ mm

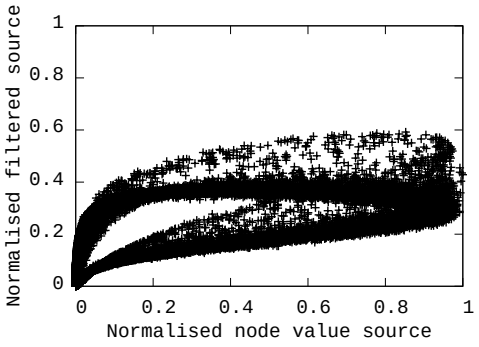

(b) $\Delta = 0.6$ mm

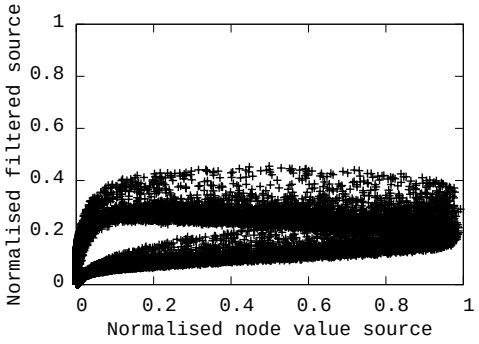

(c) $\Delta = 0.9$ mm

Figure 8: $\overline{\dot{\omega}^+}$ vs $\dot{\omega}^+(\tilde{c})$.

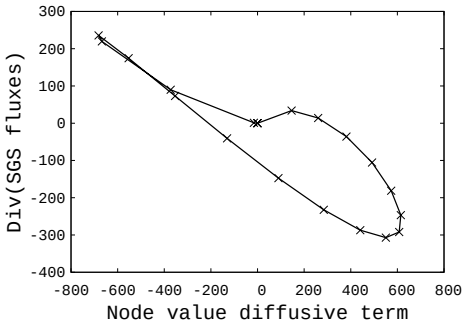

(a) $\Delta = 0.3$ mm

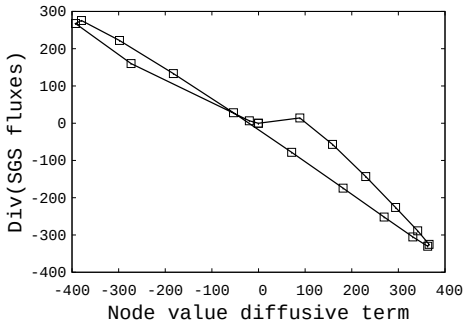

(b) $\Delta = 0.6$ mm

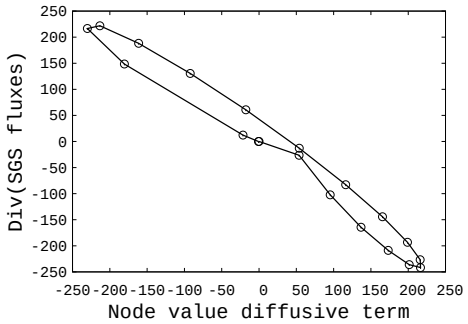

(c) $\Delta = 0.9$ mm

Figure 9: $\langle \nabla \cdot \tau \mid \tilde{c} \rangle$ vs $\langle \nabla \cdot (\overline{\rho} D_c(\tilde{c}) \nabla \tilde{c}) \mid \tilde{c} \rangle$.

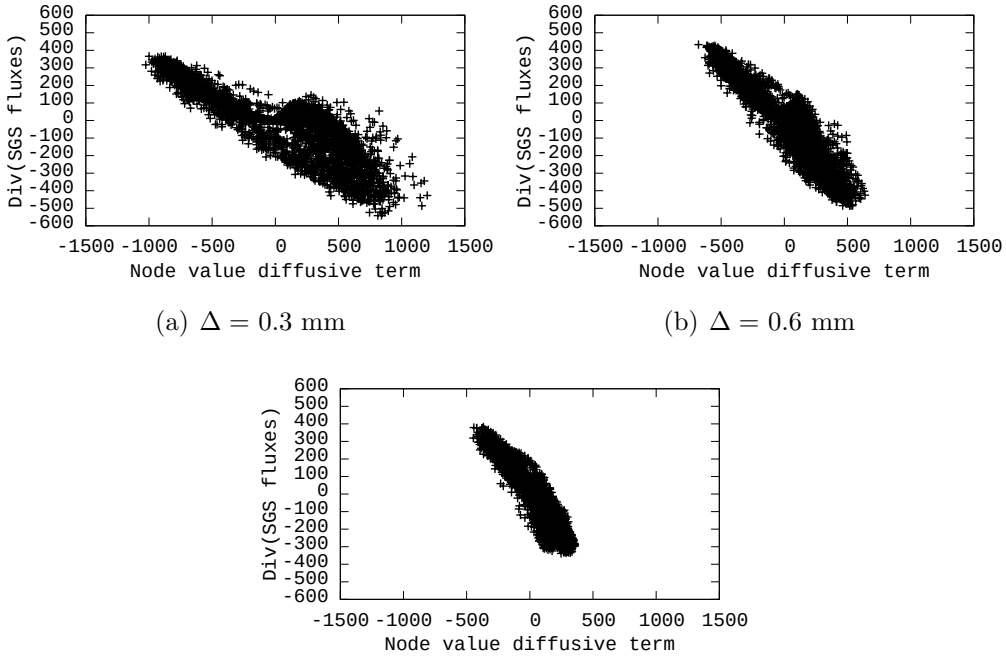

(a) $\Delta = 0.3$ mm

(b) $\Delta = 0.6$ mm

(c) $\Delta = 0.9$ mm

Figure 10: $\nabla \cdot \tau$ vs $\nabla \cdot (\overline{\rho} D_c(\tilde{c}) \nabla \tilde{c})$.

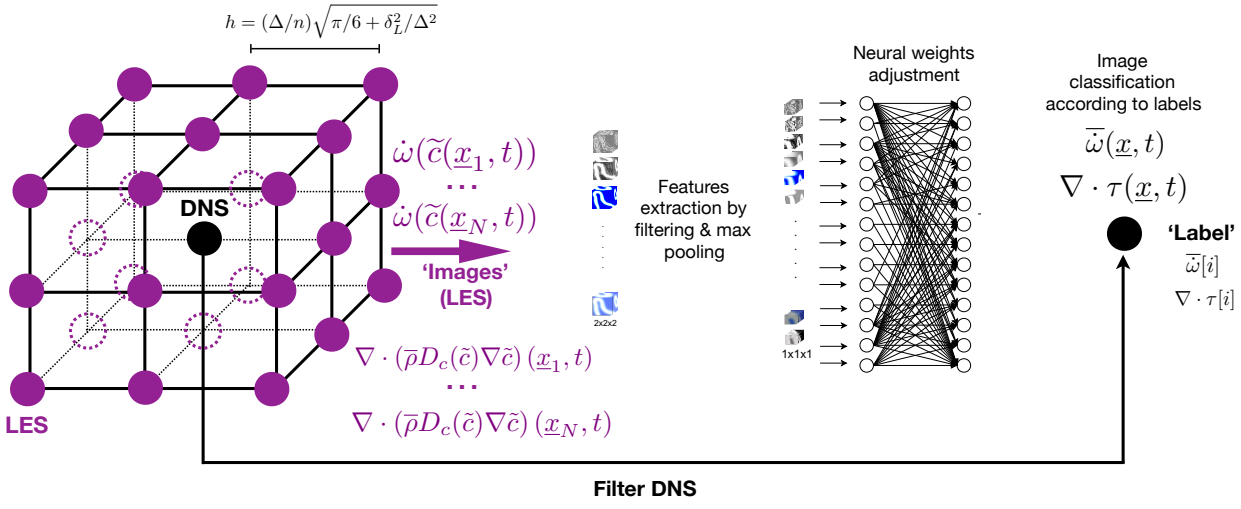

Figure 11: CNN training from DNS, sketch of the database construction.

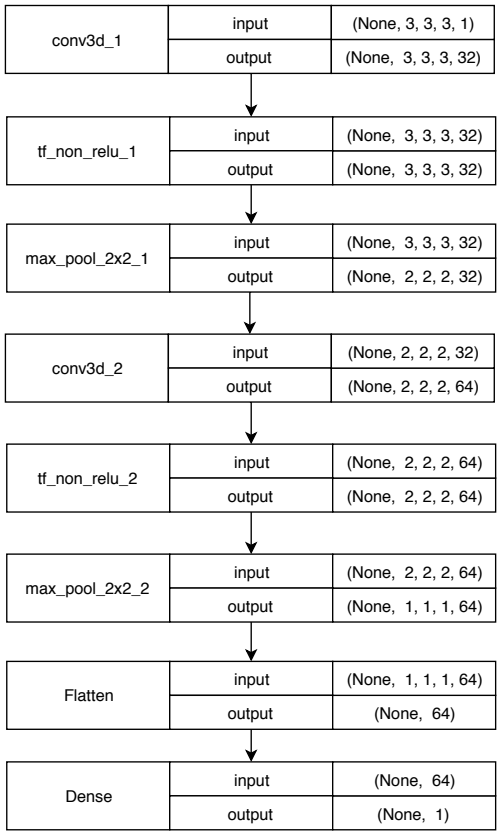

Figure 12: Structure of the convolutional neural network used (set of TensorFlow routines).

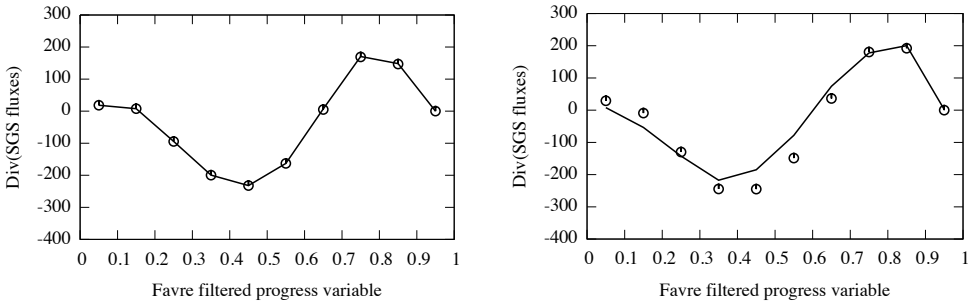

(a) $\Delta = 0.30$ mm (trained)

(b) $\Delta = 0.45$ mm (untrained)

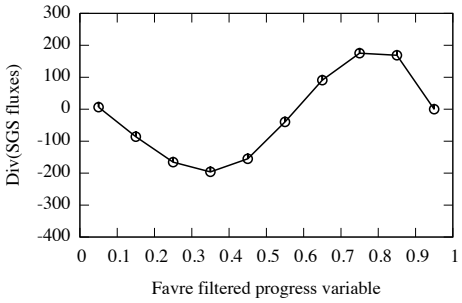

(c) $\Delta = 0.90$ mm (trained)

Figure 13: $\langle \nabla \cdot \tau \mid \tilde{c} \rangle$ vs $\tilde{c}$. Symbols: DNS reference. Line: CNN prediction.

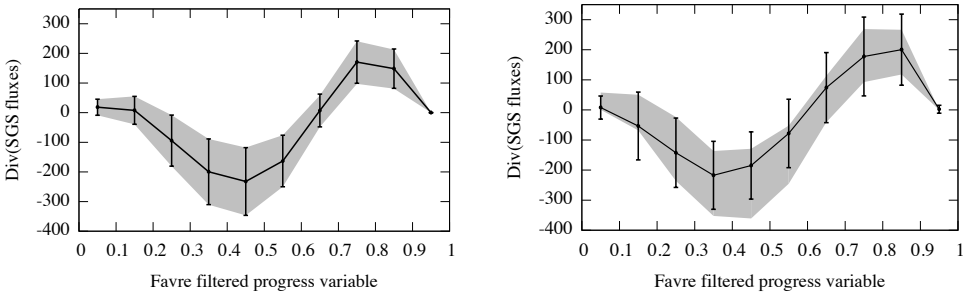

(a) $\Delta = 0.30$ mm (trained)

(b) $\Delta = 0.45$ mm (untrained)

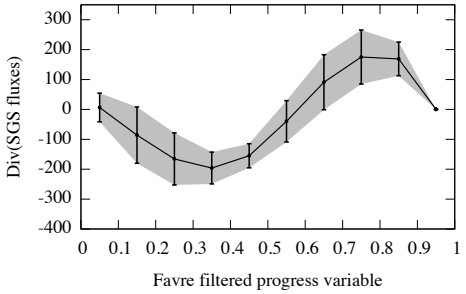

(c) $\Delta = 0.90$ mm (trained)

Figure 14: Solid line: $\langle \nabla \cdot \tau \mid \tilde{c} \rangle$ vs $\tilde{c}$ from CNN. Gray: Range covered by the signal according to the RMS in DNS, vertical bar: CNN prediction.

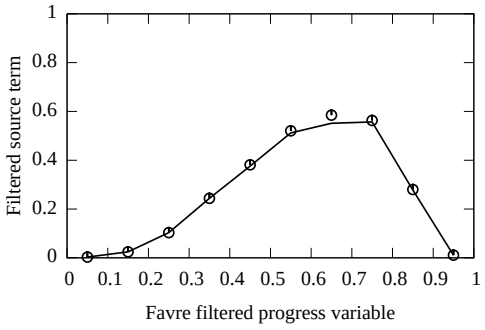

(a) Trained database. $\Delta = 0.30$ mm

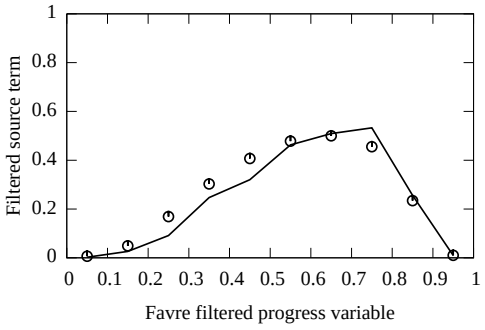

(b) Untrained database. $\Delta = 0.40$ mm

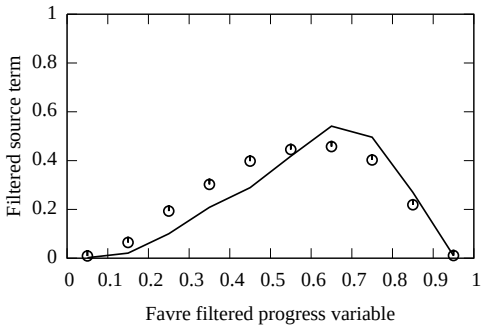

(c) Untrained database. $\Delta = 0.45$ mm

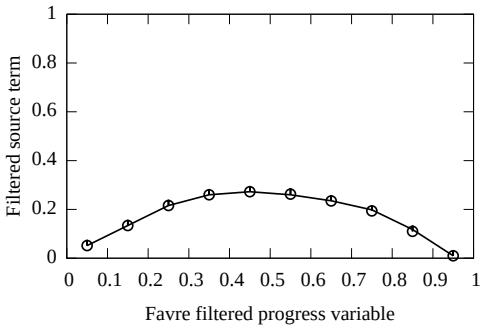

(d) Trained database. $\Delta = 0.90$ mm

Figure 15: $\left\langle \overline{\dot{\omega}^{+}} \mid \tilde{c} \right\rangle$ vs $\tilde{c}$. Symbols: DNS reference. Line: CNN prediction.

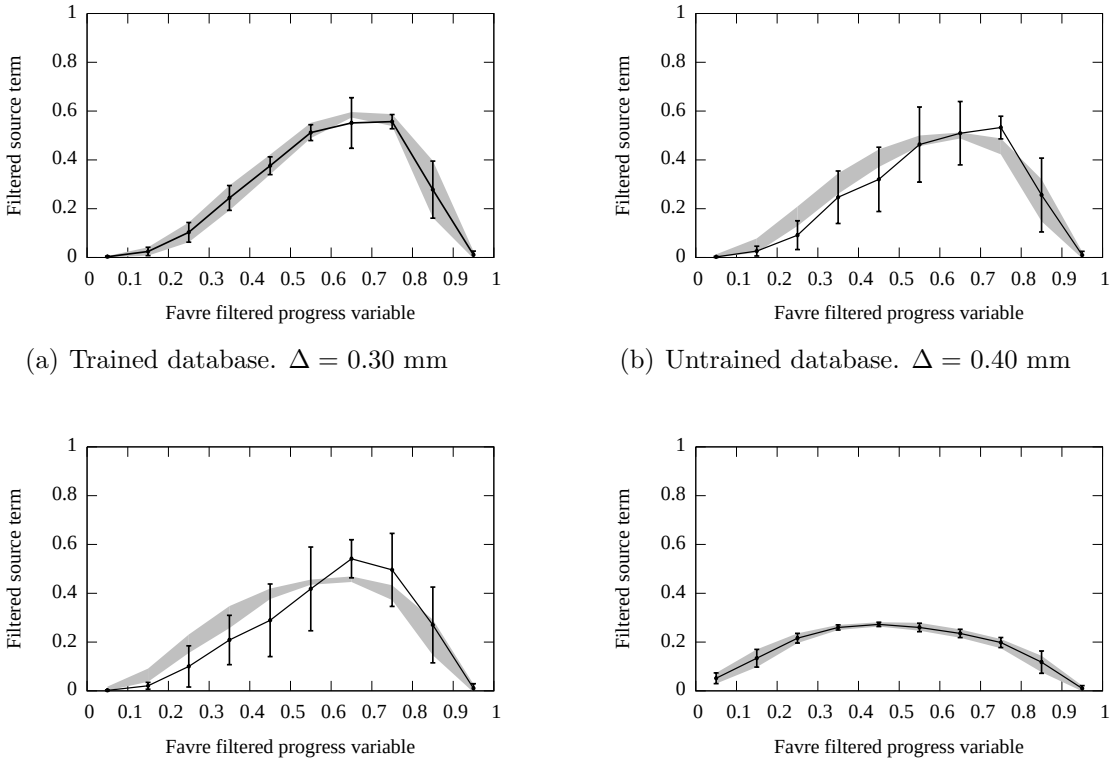

(a) Trained database. $\Delta = 0.30$ mm

(b) Untrained database. $\Delta = 0.40$ mm

(c) Untrained database. $\Delta = 0.45$ mm

(d) Trained database. $\Delta = 0.90$ mm

Figure 16: Solid line: $\left\langle \overline{\dot{\omega}^+} \mid \tilde{c} \right\rangle$ vs $\tilde{c}$ from CNN. Gray: Range covered by the signal according to the RMS in DNS, vertical bar: CNN prediction.